machines

MDPI

Article

An Inverse Kinematics Approach for the Analysis and Active Control of a Four-UPR Motion-Compensated Platform for UAV–ASV Cooperation

Pedro Pereira [1,*], Raul Campilho [2,3] and Andry Pinto [1,4]

[1] Faculdade de Engenharia da Universidade do Porto, 4200-465 Porto, Portugal
[2] Instituto Superior de Engenharia do Porto, 4200-072 Porto, Portugal
[3] INEGI, Pólo FEUP, 4200-465 Porto, Portugal
[4] INESC TEC, Pólo FEUP, 4200-465 Porto, Portugal
* Correspondence: pedro.arrojado.pereira@gmail.com

Abstract: In the present day, unmanned aerial vehicle (UAV) technology is being used for a multitude of inspection operations, including those in offshore structures such as wind-farms. Due to the distance of these structures to the coast, drones need to be carried to these structures via ship. To achieve a completely autonomous operation, the UAV can greatly benefit from an autonomous surface vehicle (ASV) to transport the UAV to the operation location and coordinate a successful landing between the two. This work presents the concept of a four-link parallel platform to perform wave-motion synchronization to facilitate UAV landings. The parallel platform consists of two base floaters connected with rigid rods, linked by linear actuators to a top mobile platform for the landing of a UAV. Using an inverse kinematics approach, a study of the position of the cylinders for greater range of motion and a workspace analysis is achieved. The platform makes use of a feedback controller to reduce the total motion of the landing platform. Using the robotic operating system (ROS) and Gazebo to emulate wave motions and represent the physical model and actuator system, the platform control system was successfully validated.

Keywords: parallel manipulator; unmanned aerial vehicle; inverse kinematics; screw theory; reciprocal screws; PID controller; robot operating system; wave-motion synchronization

Citation: Pereira, P.; Campilho, R.; Pinto, A. An Inverse Kinematics Approach for the Analysis and Active Control of a Four-UPR Motion-Compensated Platform for UAV–ASV Cooperation. *Machines* **2023**, *11*, 478. https://doi.org/10.3390/machines11040478

Academic Editors: Octavio Garcia-Salazar, Anand Sanchez-Orta and Aldo Jonathan Muñoz-Vazquez

Received: 7 March 2023
Revised: 10 April 2023
Accepted: 11 April 2023
Published: 14 April 2023

1. Introduction

Closed-loop mechanisms are parallel manipulators of a fixed and a moving platform connected by a set of kinematic chains [1]. The main advantages of a parallel manipulator are its high stiffness, compact size, capability for control with large bandwidth, robustness against external force and error accumulation, high dexterity, and suitability for accurate positioning systems [2]. The downsides of this type of mechanism are its limited workspace, and, because of the nonlinearity and complexity of the equations, a forwards dynamics solution is very challenging and complex to obtain. Concerning the design process of robotic mechanisms, serial kinematic chains are somewhat limited in their arrangements for a given motion pattern. This is not true for parallel mechanisms, which can have a very large variation of arrangements for a given motion pattern [3]. Some of the more famous examples of closed-chain mechanisms can be found in the Delta robot or the Stewart–Gough platform [4], illustrated in Figure 1. Evaluation of the degrees of freedom (DoF) of the end-effector constitutes one of the core issues in free-motion analysis of parallel mechanisms. In contrast to serial mechanisms, classical approaches, such as the traditional Kutzbach–Grübler criterion, are not valid for certain complex spatial parallel mechanisms [5]. According to the work of Merlet [6], the most widely used methods for structural synthesis of parallel mechanisms are divided into three main approaches, namely, graph theory, group theory, and screw theory. Kong and Gosselini [7] later introduced the

concept of virtual chains for the type synthesis of parallel mechanisms. These authors also performed a mobility analysis using the screw-theory-based virtual-chain approach for numerous of different possible configurations of parallel robots. The theory of reciprocal screws was first introduced by Zhao et al. [8] and has since been used in many other works related to the field of parallel mechanisms and DoF estimation problems [9–11]. Regarding the development of parallel manipulators, there is a need to identify the workspace of these mechanisms, which frames the reachable positions of the centroid of the end-effector. The workspace of a parallel manipulator imposes limitations that depend on its practical application [12]. Determining the boundary of a workspace typically relies on the manipulator's pose parameter discretization. To establish the set of possible, reachable positions, the joint limits and a kinematic model of the mechanism must be established. This can be accomplished with either forward kinematics [13] or inverse kinematics [14] approaches. Due to the multiple limbs of parallel mechanisms, solutions for forward kinematics require numerical problem-solving, while inverse kinematics can be solved analytically [15]. Parallel manipulators have seen a wide variety of applications in different fields [16,17]. The advantages provided by parallel mechanisms potentiate the application of robotics for numerous applications, such as Jones and Dunlop's proposal of a closed-loop mechanism for satellite trackers [18]. Wapler et al. [19] used a Stewart platform to design a high-precision surgery mechanism with an accuracy of 20 µm.

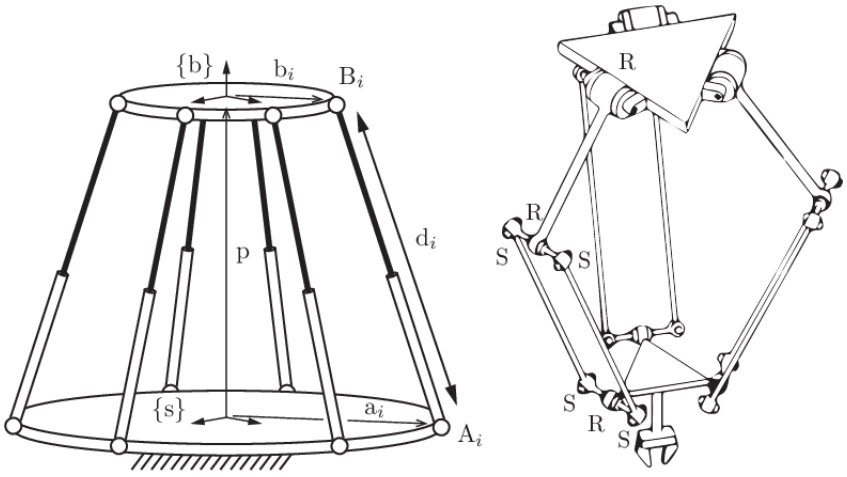

(a) Stewart–Gough platform. (b) Delta robot.

Figure 1. Popular parallel mechanisms [1].

Compared to traditional power generators on land, offshore wind energy technology presents the benefit of collecting more power due to stronger winds and the absence of landscape effects [20]. However, since offshore structures have difficult accessibility, implementation and maintenance can be time-consuming and costly [21]. Under these conditions, to reduce costs and avoid hazard to humans, underwater vehicles and inspection UAVs are an attractive option. Intervention autonomous underwater vehicles can be used together with imaging systems for inspection [22] and robotic arms for repairing [23]. UAVs can be equipped with imaging systems and perform pre-established paths for the inspection of critical parts of the structure [24]. Nonetheless, these technologies are yet in an incipient stage of evolution [25]. For offshore operations, UAVs often need a place to land closer to the structure, which ASVs could potentially provide. The motion caused by waves is mostly unpredictable, and, depending on sea conditions, it can produce large displacements of roll, pitch, yaw, sway, surge, and heave motions on a surface vehicle. Being so highly dependent on the weather and sea conditions, working in offshore environments often leads to a low working efficiency and economic loss due to unworkable conditions. The recent literature has explored the potential for cooperation between ASVs and UAVs in the automatic launch and recovery of the UAVs. These applications usually

employ vision techniques, so the UAV is capable of detecting the landing pad located on an ASV. However, these techniques are still vulnerable to highly dynamic sea states [26]. To overcome the difficulties of landing the UAV, Li et al. [27] developed an ASV with an attitude-prediction controller designed by a bidirectional long-short term memory neural network and a proportional–integral–derivative (PID) pose controller for the UAV to guarantee real-time synchronization movement of the UAV–ASV. Their results showed that this type of cooperation effectively improves the landing accuracy. Furthermore, Liu et al. [28] explored the potential of parallel mechanisms for UAV landings in highly uneven and unstructured land terrain using a three-RRR-limb parallel mechanism that functions both as a manipulator and as adaptive landing gear. Outside the UAV-related research, some attempts at wave-motion compensation using parallel mechanisms are exemplified in the work of Guo et al. [29], which proposes a 4-CPS/RPS parallel mechanism with a classic PID controller to mitigate wave motion induced in a ship. Chen et al. [30] proposed a parallel manipulator driven by pitch and roll active motion compensation with a fuzzy sliding mode controller and a PID controller to diminish the risk of humans getting in and out of offshore wind turbine structures. Cai et al. [31] studied the concept of a ship-mounted Stewart platform for equipment such as cranes and drilling platforms to eliminate the effect of wave-induced ship motions, effectively increasing the workable time for offshore installations. A common issue many of these works face is that, due to the variability of sea conditions, a controller system may be adequate for a given sea state and inadequate for others.

The ATLANTIS project [32] aims to establish an infrastructure to allow the demonstration of key enabling robotic technologies for the inspection and maintenance of offshore wind turbines. One of the focuses of this project is the use of UAVs for blade inspection. Considering the distance of offshore structures to shore and the limited capabilities of UAV batteries it is necessary for UAVs to be recovered near the mission site after completing the inspection. Considering the set of advantages offered by a parallel mechanism, this work proposes a novel motion-compensated four-UPR parallel platform designed for the autonomous landing of UAVs in offshore environments based on the theory of reciprocal screws. There has been some work dedicated to a four-UPU parallel mechanism, which has Shöenflies type-motion (three translations plus one rotation) [33]. However, for the intended purposes, the platform presented in this work only needs two rotations around the x and y-axis to compensate for wave motions and one translation along the z-axis to position the landing platform. Thus, a variation of the four-UPU platform is introduced with the four UPR limbs. This variation is not described in the literature. Parallel mechanisms with fewer than six DoFs excel in terms of simpler structure, easier control, and lower cost. While this mechanism can be achieved with three limbs, a fourth one adds more rigidity and maintains the symmetry of the ASV. Having a permanently horizontal platform to land, the UAV is much less susceptible to land in an uneven position and topple, possibly damaging its sensors/structure or, in a worst case scenario, falling overboard. The first tests of this platform are to be conducted at the ATLANTIS test centre's buoy DURIUS. DURIUS is close to the coast, so the wave dynamics will not be as harsh as in offshore environments. To test the concept of the four-UPR mechanism for different wave states, this work implements a PID controller to establish a baseline performance, which provides a good solution for these conditions. This work addresses the difficult task of safely launching and recovering a UAV on a landing pad influenced by wave motions. The implementation of this platform offers more flexibility in UAV–ASV cooperative missions for offshore wind-turbine inspection.

This work is organized as follows: In Section 2, the problem and platform mechanism presented in this paper are described, as well as a DoF analysis based on the theory of reciprocal screws. Section 3 describes the systematic approach and solution for the inverse kinematics of a four-UPR parallel mechanism. From this solution, the limb lengths, position, and velocity of the passive joints are obtained for any given position and orientation of the mobile platform. Section 4 details the workspace and limits the analysis of the platform.

Section 5 presents the platform-simulation environment and the results of the implemented PID controller. Finally, Section 6 provides a discussion of the proposed work.

2. Platform Description

2.1. Problem Statement

One of the greatest limitations in UAV–ASV cooperative motions is in landing the UAV safely in highly dynamic sea states. Wave-motion compensation has been a topic of research for some time; however, there have been few attempts at tackling the issue of landing UAVs on a platform at sea. This is a difficult task, since highly dynamic waves and wind will induce significant angular displacements on the platform, and a bad landing can be devastating for the UAV. In this work, we attempt to tackle this challenge using a parallel mechanism that is capable of maintaining a horizontal position while the drone is trying to land. Consider the mission illustrated in Figure 2. Here, the main steps of the mission are as follows: the UAV takes off from the platform near the structure; it performs the inspection of the structure and registers relevant data using sensors, such as visual cameras and LiDARs (light detection and ranging); upon completing the inspection, the drone returns to the ASV using a perception system that combines visual, thermal, and three-dimensional LiDAR to detect an ArTuga equipped on the ASV [34]; once detected, the UAV attempts to land on the ASV's platform. This work addresses the first and last steps, which involve the launch and recovery of the UAV.

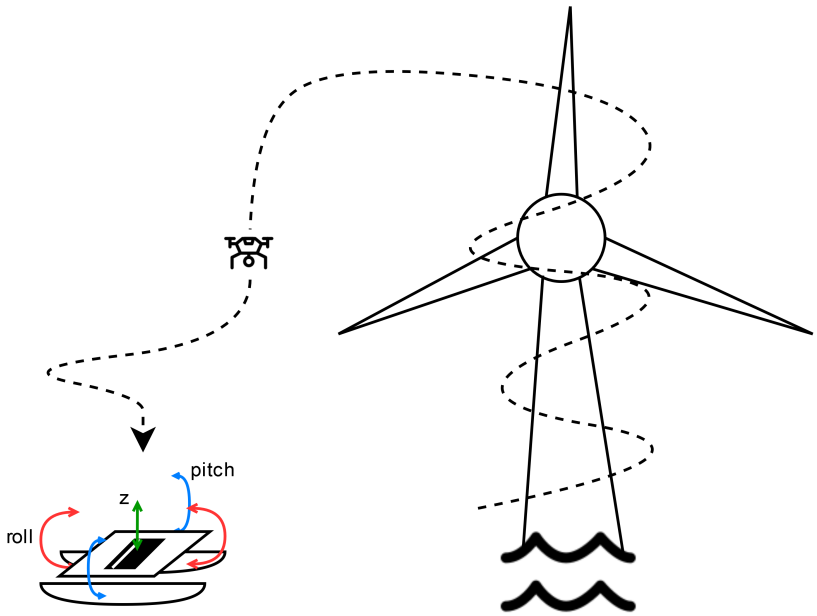

Figure 2. UAV–ASV cooperation for inspection and maintenance of offshore wind turbines. Mission schematic.

The proposed ASV has a 4-UPR mechanism depicted in Figure 3 with a top mobile platform for the landing of UAVs linked to the floating base platform with four limbs. Each limb consists of a revolute joint (R-joint), followed by a prismatic joint, and ending in a universal-joint (U-joint). The limb length is characterized by l_i. This mechanism is capable of translational movement along the z-axis and rotational movements along the x- and y-axis. The orientation and position of the platform is provided by an inertial measurement unit (IMU) installed in the base platform. The centre point of the global coordinate system is located at origin O (centre of the base platform).

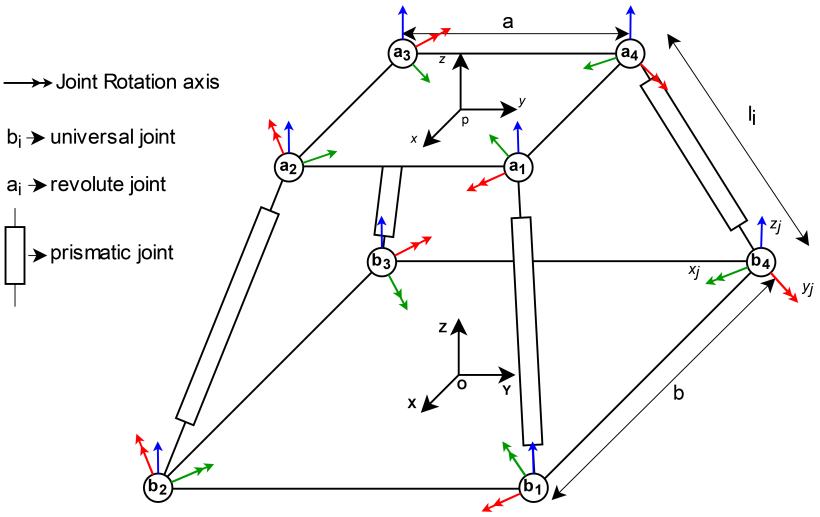

Figure 3. The 4-UPR platform mechanism schematics.

The top and bottom joints of the platforms form a square with side a and b, respectively. The z-axis is perpendicular to the platform, and the x-axis and y-axis are oriented in such a way that the positions of the b_i joints are given by:

$$\begin{aligned} b_1 &= \begin{bmatrix} b/2 & b/2 & 0 \end{bmatrix}^T \\ b_2 &= \begin{bmatrix} b/2 & -b/2 & 0 \end{bmatrix}^T \\ b_3 &= \begin{bmatrix} -b/2 & -b/2 & 0 \end{bmatrix}^T \\ b_4 &= \begin{bmatrix} -b/2 & b/2 & 0 \end{bmatrix}^T \end{aligned} \tag{1}$$

It is assumed that a_i is the position of the upper platform joints relative to the origin frame. The mobile frame of reference, p, located at the centre of the upper platform, is oriented with the Z-axis perpendicular to the mobile platform, and the X-axis and Y-axis are oriented in such a way that the positions of the a_i joints relative to p are:

$$\begin{aligned} pa_1 &= \begin{bmatrix} a/2 & a/2 & 0 \end{bmatrix}^T \\ pa_2 &= \begin{bmatrix} a/2 & -a/2 & 0 \end{bmatrix}^T \\ pa_3 &= \begin{bmatrix} -a/2 & -a/2 & 0 \end{bmatrix}^T \\ pa_4 &= \begin{bmatrix} -a/2 & a/2 & 0 \end{bmatrix}^T \end{aligned} \tag{2}$$

For a proper workspace definition, the limits of each joint need to be established. The prismatic joint is representative of an electric actuator with a retracted cylinder size of 0.7225 m, with a stroke of 0.4 m, defining l_i as $0.7225 \geq l_i \geq 1.1225$ m. The angle between the two parts that constitute a U-joint can be represented by $\beta_i = \begin{bmatrix} roll & pitch & 0 \end{bmatrix}$, where roll and pitch represent the angle around the local joint frame's x_i and y_i axis, respectively. The U-joint roll and pitch angles can be defined by the dot product of the limb frame x- and y-axis with the joint frame x- and y-axis. The limb frame is a rotation of the joint frame, where z is axial to the limb. The joint limit established for the U-joints is 30 degrees, as it is a common limit in standard models, defining β as $-45 \geq \beta \geq 45$ degrees.

As shown in Figure 4, the base platform consists of two floaters connected by rigid rods. The U-joint's position at the base, b_i, and the R-joint's position at the upper platform are adjustable, so the length of a and b can be optimized for greater mobility and angular velocity. A key point for establishing the configuration of the centroid p is the position in the global frame Z-axis. A lower centre of gravity will allow the platform not to topple with more aggressive wave amplitudes. Another important aspect to consider is the distance

between the platforms, in order to avoid a collision between the two bodies when rotating the top part. The top platform is a square with size 2×2 m^2. To avoid a collision, a relationship between the platform orientation and the z position of the platform needs to be established. Consider α the angle between the z'-axis and z-axis of the frame p, where the z-axis is the z-vector of the platform initial orientation, given by $\begin{bmatrix} 0 & 0 & 1 \end{bmatrix}$, and the z' vector is the z-axis after a rotation. Thus, α can be obtained by the dot product of z and z' as:

$$\alpha = \arccos \frac{z \cdot z'}{\|z\| \times \|z'\|} \qquad \|z\| > \sin(\alpha) \times \sqrt{2} \tag{3}$$

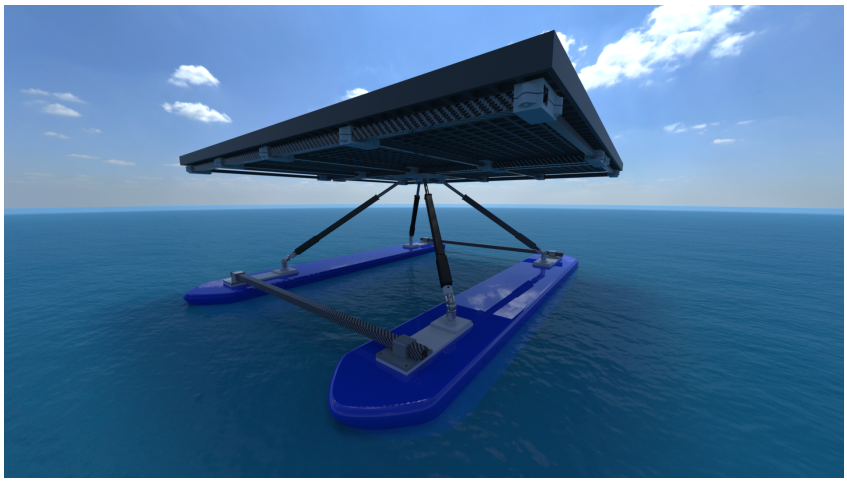

Figure 4. 3D model of the 4-UPR platform mechanism.

2.2. Degree of Freedom Estimation

To determine the quantity, type, and direction axes of the end-effector DoFs for the 4-UPR platform presented in this work, the applied method relies on screw theory and reciprocal screw systems. In this method, the constraint space of the end-effector is studied according to the terminal constraint space of its kinematic chains. As previously mentioned, this method was first developed by Zhao et al. [8]. A more mature demonstration is presented in the book by the same author [5]. Let us consider the kinematic chain presented in Figure 5, which represents the i^{th} limb of the platform.

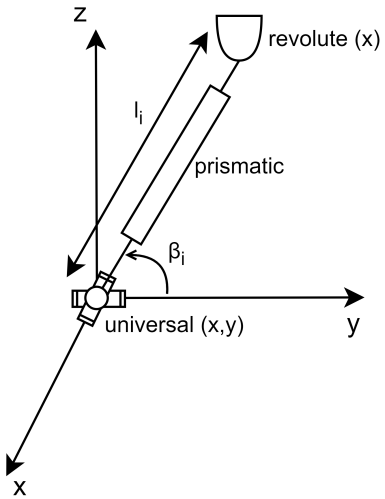

Figure 5. Kinematic chain of the i^{th} limb of the platform.

The Plücker coordinates of the kinematic pair of the joints belonging to the limb can be written as:

$$\$_1 = \begin{bmatrix} 0 & 1 & 0; & 0 & 0 & 0 \end{bmatrix}^T \tag{4}$$

$$\$_2 = \begin{bmatrix} 1 & 0 & 0; & 0 & 0 & 0 \end{bmatrix}^T \tag{5}$$

$$\$_3 = \begin{bmatrix} 0 & 0 & 0; & 0 & \cos\beta_i & \sin\beta_i \end{bmatrix}^T \tag{6}$$

$$\$_4 = \begin{bmatrix} 1 & 0 & 0; & 0 & -l_i \times \sin\beta_i & l_i \times \cos\beta_i \end{bmatrix}^T \tag{7}$$

Now, the Plücker coordinates of the limb, $\$_{l_i}$, are defined as:

$$\$_{l_i} = \begin{bmatrix} \$_1 & \$_2 & \$_3 & \$_4 \end{bmatrix}^T \tag{8}$$

According to reciprocal screw theory, two screws that satisfy Equation (9) are a pair of reciprocal screws. According to the physical meaning of reciprocal screws, the reciprocal of $\$_{l_i}$ denotes the constraints forces applied to the kinematic chain.

$$\$^T \Delta \$^r = 0 \tag{9}$$

$$\Delta = \begin{bmatrix} 0 & I \\ I & 0 \end{bmatrix} \tag{10}$$

where Δ is a 6×6 matrix. The solution for $\$^r_{l_i}$ can be obtained with linear algebra methods.

$$\$^r_{l_i} = \begin{bmatrix} 1 & 0 & 0; & 0 & 0 & 0 \\ 0 & 0 & 0; & 0 & 0 & 1 \end{bmatrix}^T \tag{11}$$

which denotes a pure couple that is parallel to the z-axis and a force parallel to the x-axis. The movement constrained by $\$^r_{l_i}$ is given by $\$^m_{l_i} = \begin{bmatrix} 0 & 0 & 1; & 1 & 0 & 0 \end{bmatrix}^T$, denoting a rotation parallel to the z-axis and a translation along the x-axis. In the global frame of reference, $O - XYZ$ (see Figure 3), the constrained motion screw can be represented as:

$$\$^m_{l_i} = \begin{bmatrix} 0 & 0 & 1; & \cos\alpha_i & \sin\alpha_i & 0 \end{bmatrix}^T \tag{12}$$

where α_i is the angle of the local x-axis of the i^{th} limb to the global frame of reference. The constraints of the end-effector are directly related to the terminal constraints of the kinematic chains. It is possible to find the constraints of the end-effector by analysing the span ($\$^C_P$) of its constrained motions:

$$\$^C_P = span\left\{ \begin{bmatrix} \$^m_{l_1} & \$^m_{l_2} & \$^m_{l_3} & \$^m_{l_4} \end{bmatrix}^T \right\} \tag{13}$$

$$\$^C_P = \begin{bmatrix} 0 & 0 & 1; & 0 & 0 & 0 \\ 0 & 0 & 0; & 1 & 0 & 0 \\ 0 & 0 & 0; & 0 & 1 & 0 \end{bmatrix} \tag{14}$$

The DoF of a mechanism are given by $F = 6 - d$, where d is the number of dimensions that all the reciprocal screws can be spanned in the normal linear spaces. It is clear that this parallel mechanism has 3 DoF and can rotate about the X and Y-axis and translate in the Z-axis.

3. Inverse Kinematics

Inverse kinematics refers to the construction of the kinematic equations, so that, for a given end-effector position, the joint variables can be established. The orientation of the upper platform is defined by a rotation matrix around the roll (θ_x) and pitch (θ_y) angles, provided by an IMU on the bottom platform. Since it is not possible, nor advantageous, to

control the yaw of the platform, it is assumed that θ_z is always zero. The rotation matrix is given by:

$$R = \left[R_y R_x\right] = \begin{bmatrix} c\theta_y & s\theta_x \times s\theta_y & s\theta_y \times c\theta_x \\ 0 & c\theta_x & -s\theta_x \\ -s\theta_y & c\theta_y \times s\theta_x & c\theta_y \times c\theta_x \end{bmatrix} \tag{15}$$

where c and s are the cosine and sine trigonometric functions. Considering the DoFs of the platform, at any time instance, the state of the upper platform can be represented with the orientation θ and the centroid position P, in global coordinates, given by:

$$\begin{aligned} P &= \begin{bmatrix} 0 & 0 & P_z \end{bmatrix} \\ \theta &= \begin{bmatrix} \theta_x & \theta_y & 0 \end{bmatrix} \end{aligned} \tag{16}$$

The position of the upper U-joints, a_i, can be solved as:

$$a_i = P + R \times pa_i \tag{17}$$

Substituting Equations (2), (15), and (16) in Equation (17) gives the position of all top platform joints. Since the lower U-joint's position is a known constant, the length of each limb (l_i) can be determined as:

$$l_i = \sqrt{[a_i - b_i][a_i - b_i]^T} \tag{18}$$

This parameter defines the necessary length of the prismatic cylinders, and therefore the control input, for the desired platform position and orientation. The vector that represents the i^{th} limb is given by:

$$S_i = a_i - b_i \tag{19}$$

The unit vector that defines the i^{th} limb is:

$$s_i = S_i / l_i \tag{20}$$

Considering $\dot{\theta} = [\dot{\theta}_x, \dot{\theta}_y, 0]^T$ as the angular velocity and $\dot{P} = [0, 0, \dot{P}_z]^T$ the linear velocity of the centroid p, the velocity of each limb can be determined as:

$$\dot{S}_i = \dot{\theta} \times a_i + \dot{P} \tag{21}$$

The sliding velocity, given by the velocity component along the limb, can be determined as:

$$\dot{l}_i = s_i \cdot \dot{S}_i \tag{22}$$

The inverse kinematics analysis enables the study of how the different design parameters of the platform influence the constrictions of movement. The different design parameters are considered as:

- Side a of the top platform, which denotes the position of the top joints. Smaller values of a mean more angular movement is achieved for shorter strokes, which can be explored to compensate for slower linear actuators. On the other hand, small values of a can lead to some instability regarding the stiffness of the mobile platform.
- Side b of the base platform, which denotes the position of the bottom joints. By distancing the bottom joints from one another, it is expected that the mechanism is more stable for harsher dynamic conditions. However, the steepness of the linear actuators also influences the angular speed of the mobile platform.
- Position along the Z-axis. This design parameter is adaptable even after construction, as it depends entirely on the linear actuator's stroke position. The major influence of this parameter is on the joints and collision limits of the mobile platform, and the position of the centre of mass of the mechanism.

4. Workspace Analysis

The workspace of a robot is defined by the volume of space reachable by its end-effector. For this parallel mechanism, let us consider that the end-effector is defined by the upper platform's centroid, p, and the position of the top joints, a_i. Due to the nature and application of this mechanism, it is not necessary to control the z-position while compensating for the wave motions. However, due to the limits of the platform, be it either through collision within itself or the joint limits established in Section 2, the position of the platform in the Z-axis can be studied to conciliate the platform stability with the range of motion. Using the inverse kinematics analysis performed in Section 3, the joints and platform positions, as well as the limbs length and orientations, can be calculated. The bottom U-joint angles, β, can be obtained through the s_i unit vectors:

$$s_i = \begin{bmatrix} s_{xi} & s_{yi} & s_{zi} \end{bmatrix} \tag{23}$$

$$\beta_{xi} = \arccos(s_{xyi} \cdot s_i) \tag{24}$$

$$s_{xyi} = \frac{\begin{bmatrix} s_{xi} & s_{yi} & 0 \end{bmatrix}}{\left\| \begin{bmatrix} s_{xi} & s_{yi} & 0 \end{bmatrix} \right\|} \tag{25}$$

$$\beta_{yi} = \arccos(s_{xyi} \cdot \begin{bmatrix} 0 & 1 & 0 \end{bmatrix}) - \frac{\pi}{4} \tag{26}$$

In Equation (26) we subtract $\pi/4$, since the local y-axis of the joint is at 45 degrees to the global Y-axis. Due to the disposition of the platform and the symmetrical nature of the joint's disposition the top platform R-joint angles, γ_i, can be obtained as:

$$\gamma_i = \arccos\left(\frac{p - a_i}{\|p - a_i\|} \cdot s_i\right) \tag{27}$$

The superscript "$(\cdot)^0$" refers to the initial time instance. For the workspace analysis, the required numerical elements are the size of a and b and the position of z^0, as well as the limits of each joint. The workspace of the platform at position z^0 can be defined through a sweep, where the limits are computed through each iteration of possible roll and pitch combinations. To ease the computation load, the limits for non-composite movements (only roll or only pitch) were first determined for $z^0 = 0.5$ m, $a = 0.2$ m, and $b = 1.25$ m. The choice of z^0 is determined by the maximum angle required to stabilize the upper platform for a specific wave height. To determine the optimal value of z^0, an iterative process was performed using the simulator presented in Section 5. Considering the roughest wave parameters used in the simulations, in a sea state of 3 on the Douglas sea scale, this angle was found to be 20 degrees, which justifies z^0 to be 0.5 m. The results of the sweep are shown in Table 1. For this mechanism, the limits of the roll and pitch of the end-effector are identical. In addition, the lower and upper limits are symmetrical.

Table 1. Range of motion for the roll and pitch of the end-effector at $z = 0.5$ m.

Motion Variable	Range of Sweep	Verified Limit	Units
Pitch	$-\pi/2$ to $\pi/2$	$-\pi/9$ to $\pi/9$	rad
Roll	$-\pi/2$ to $\pi/2$	$-\pi/9$ to $\pi/9$	rad

For the set values of z^0, a, and b described above, the workspace of the upper platform a_i U-joints can be seen in Figure 6. The edges of the upper platform (2×2 m^2) are represented by a green outline in Figure 6a. For better clarification, the same plot can be observed in Figure 6b, with more resolution and without the edges. The projected 2D range of motion of the U-Joint a_1 can be seen in Figure 7.

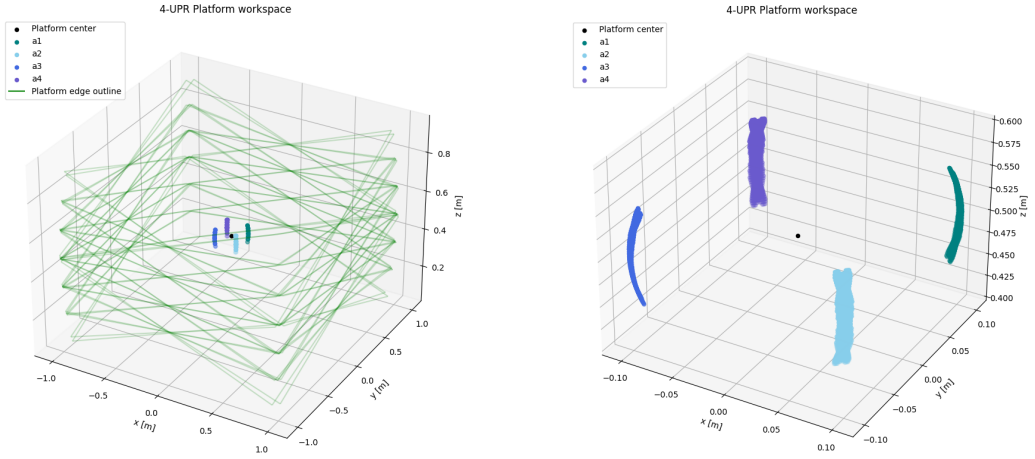

(**a**) (**b**)

Figure 6. Workspace analysis of a 4-UPR platform for $z = 0.5$ m: (**a**) Workspace with platform outline; (**b**) Workspace without platform outline.

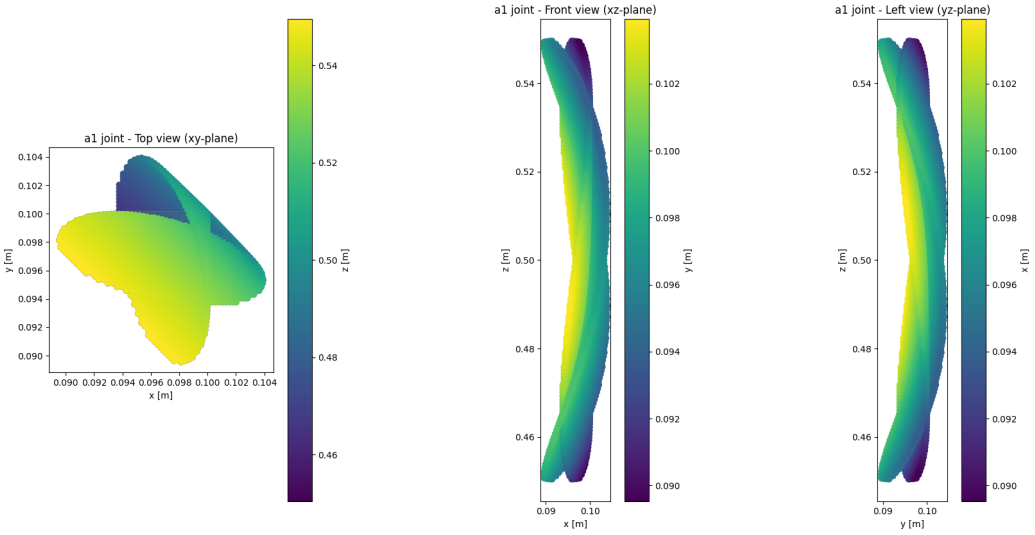

Figure 7. Workspace analysis for optimum configurations projected in 2D space for $z = 0.5$ m.

The workspace of the platform shows that the limits of the roll and pitch of the platform change with one another. For example, in an orientation where the platform has a pitch of $\pi/9$ degrees, the roll limit is at 0 degrees. This relationship can be analysed with a sweep, where the resulting plot can be seen in Figure 8b. The filled area shows the possible combinations for orienting the platform. That area can also be represented by Equation (28).

$$\sqrt{\theta_x^2 + \theta_y^2} \leq \frac{\pi}{9} \tag{28}$$

Due to the property of the upper and lower limits of this specific case, one can quickly identify the radius of the circle as either the pitch or roll upper limit in the case of $z^0 = 0.5$ m. The only constraint in this configuration of the mechanism is the collision between the top and bottom platforms (Equation (3)). It is correct to assume that a higher z^0 will mean a higher platform mobility, at least until the joints start reaching their limits and at the cost of a higher centre of mass, meaning less stability. This relationship is demonstrated in Figure 8a.

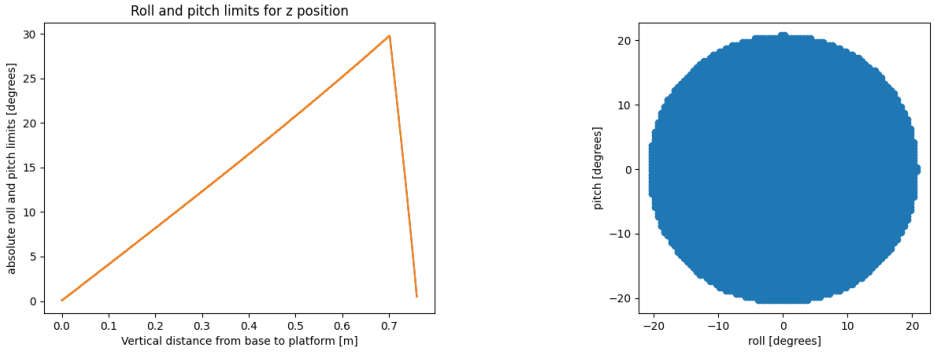

(**a**) (**b**)

Figure 8. Roll and pitch limit analysis: (**a**) Roll and pitch limit variation with distance between platforms; (**b**) Allowed platform orientation in degrees for $z = 0.5$ m.

5. Simulation and Results

To validate the design and evaluate the concept of the four-UPR platform, a demonstration is presented in a simulated environment, recurring to the ROS framework and the Gazebo simulator to model the platform joints and links and simulate the control of the mechanism and the wave motions. A screenshot of the simulator can be seen in Figure 9.

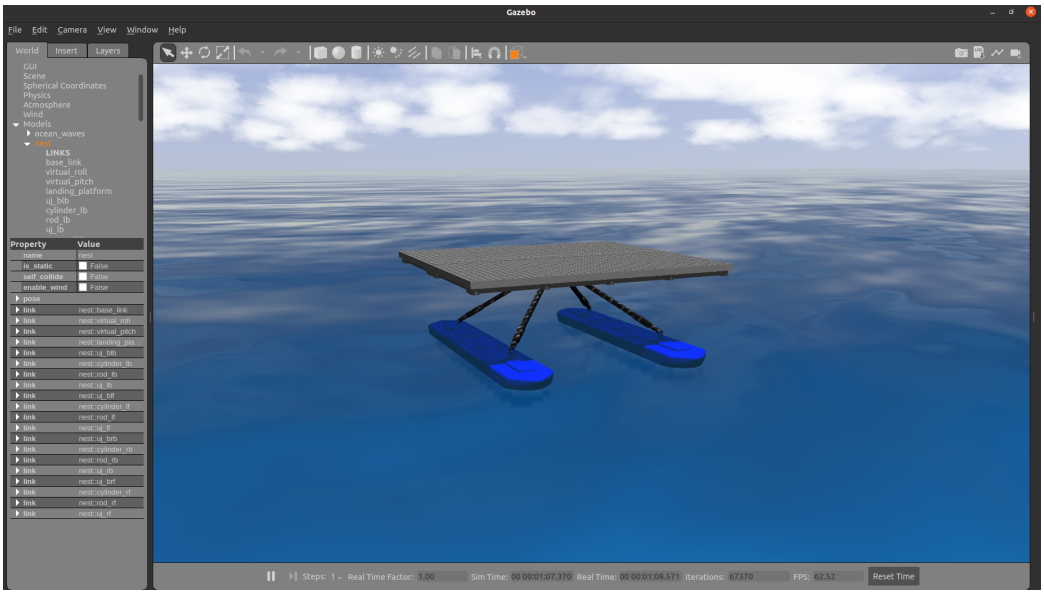

Figure 9. Screenshot of the simulator in Gazebo 11.

The robot is modelled in a Unified Robot Description Format (URDF), an XML format to represent robots. However, due to the tree-like structure of the URDF format, it is impossible to model a parallel mechanism without some workarounds. To solve this issue, a virtual chain was created to link the top platform to the bottom one, and the four kinematic chains were then connected to the top platform via a script that continuously calculates the joint angles over time using the equations described in Sections 2 and 3, recurring to static links that represent s_i^0, to have a static reference frame within the robot (see Figure 10). The virtual chain that models the top platform movement is analogous to dim $\$_P^C$ in Equation (13).

The intended purpose of the platform is to maintain the top platform in a horizontal position in an ocean surface environment. Using the information gathered by the IMU in the bottom platform, it is possible to compute the length of the prismatic actuators that, for a given orientation of the bottom platform, the top platform tends towards a horizontal position. A position controller is used for this task. The encoders on the prismatic actuators

give the current lengths of the limbs, and the data provided by the IMU and the equations described in Section 3 give the desired lengths of the limbs. The adopted control system takes the desired position and orientation of the top platform as input, and the output gives the limb's desired length, with a feedback PID controller to improve the stability and accuracy of the outputs. The PID controller was manually tuned for the simulator. The values of $k_p = 5000.0$, $k_i = 0.5$, and $k_d = 10.0$ will likely have to be adjusted for the real mechanism. A diagram of the control system can be seen in Figure 11.

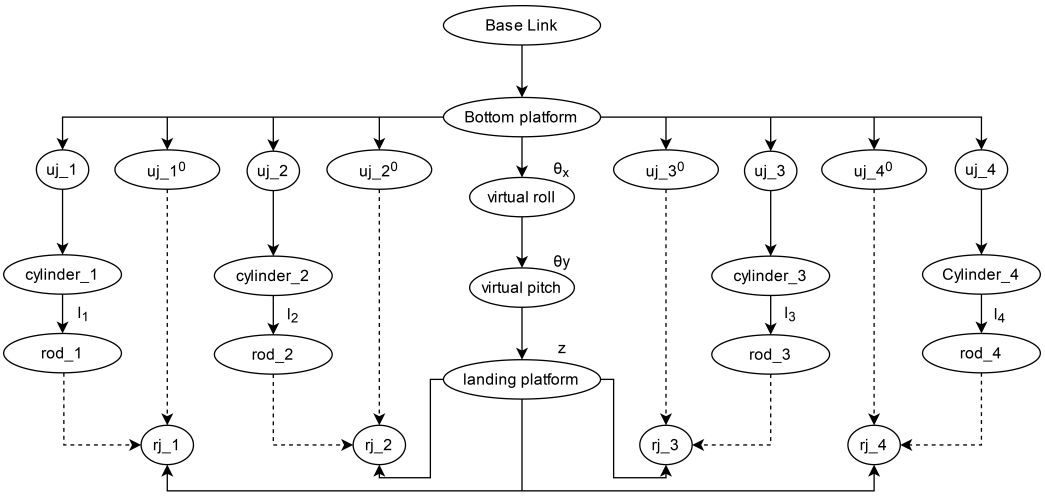

Figure 10. Tree structure of the platform links. Dashed lines—scripted connections.

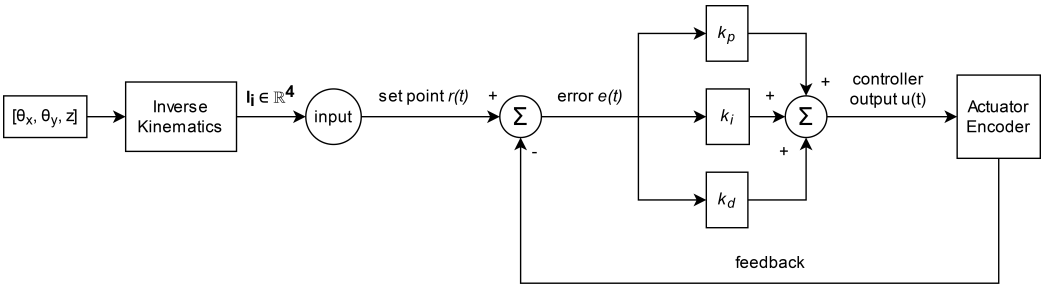

Figure 11. Control system of the 4-UPR platform.

The operational conditions of the platform are determined by several factors, including the capabilities of the UAV, the joint limits, and the sea state. The technical aiding equipment limitations, such as the support boat, also contribute to these conditions. A wave height of 1 m is defined as the the platform's operational limit, which corresponds to wave state 3 on the Douglas sea scale. Additionally, the UAV cooperating with this platform should not be operated in wind speeds exceeding 20 knots as its control starts becoming unreliable.

The maritime environment is physically simulated using the Gazebo plug-ins from Virtual Robot X [35]. The wave motions follow the model of Gerstner Waves [36] to approximate the influence of ocean waves in a simplified manner intended to balance physical fidelity and visual realism with real-time execution requirements. The motion of the bottom platform can be obtained with an IMU, which provides the orientation, angular velocity, and linear acceleration. In order to compare the movements of the top and bottom platform, another IMU is placed in the top platform. Since the control of the mechanism is executed with a position controller, the efficacy (η) of the mechanism for a given wave state and cylinder velocity is given by Equation (29), where α_{bottom} denotes the angle of the Z-axis to the Z'-axis in the global frame O, provided by the IMU. The same logic applies to α_{bottom}. Considering that the prismatic actuators have a linear speed of 0.1 m/s, which, depending on the current orientation of the platform, translates to an angular velocity up to 1.7 rad/s of the upper platform, the results for different wave states are shown in

Table 2. The selected wave parameters were based on realistic values that can be measured in the different wave states. While there is generally a correlation between wave height and period, the shorter periods for some large waves reflect how the platform may respond to rapid changes in steepness. All the tests were conducted over 30 s. The resulting plots are shown in Figure 12. The machine conducting the simulations has an i5-10600K CPU @ 4.10 GHz, a GeForce RTX 2060, and 15.5 GiB memory, running ROS Noetic and Gazebo 11.

$$\eta = \% \int_0^t \frac{\alpha_{bottom} - \alpha_{top}}{\alpha_{bottom}} dt \tag{29}$$

Table 2. Efficacy of the mechanism for different wave states.

Wave State	Number of Waves	Amplitude [m]	Period [s]	Direction [x,y]	η (%)
1	1	0.2	3	[1,1]	98.23
2	2	0.2;0.3	5;3	[1,0];[0,1]	97.16
3	3	0.2;0.3;0.4	7;5;3	[1,0];[0,1];[1,1]	94.84

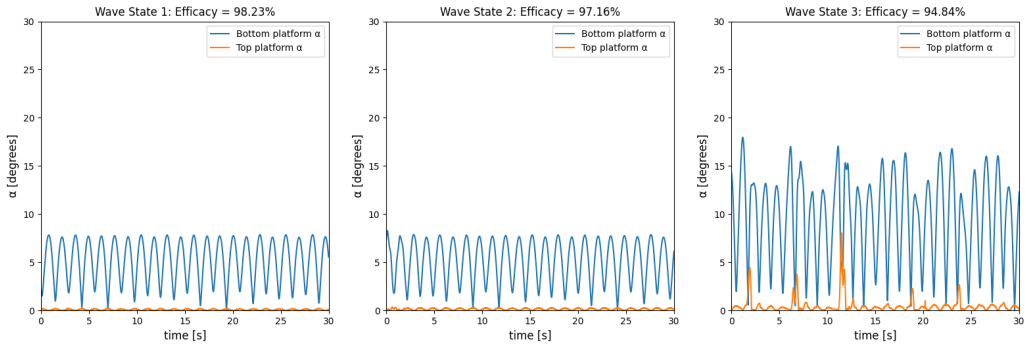

Figure 12. Resulting plots for the different wave states presented in Table 2.

Overall, the mechanism has a very good η for calmer (lower amplitudes, longer periods) wave states. However, as the waves grow more aggressive, the mechanism tends to have a much lower η. This can be attributed to three factors:

- The speed capacity of the linear actuators: with faster cylinders, the position correction can also occur faster, which will lead to less motion of the top platform. To improve the stability, one can acquire a more expensive, albeit faster, cylinder, which can be harder to control properly.
- The adopted control system: the simplicity of the adopted control system leads to poor adaptation to quick rates of change induced by waves with high amplitudes and short periods (evidenced in Figure 12). Due to tidal wave predictability and stability, and since UAVs usually do not operate well in strong winds (which cause highly irregular waves), the implementation of a predictive control system is recommended. Other studies such as that of Halvorsen et al. [37] have shown the success of this type of prediction algorithm for wave synchronization for rougher sea states.
- The small size of the vessel also implies that its roll and pitch orientation will be more affected by the wave's motion. Thus, a bigger vessel could also provide better stability.

6. Discussion

This paper presented a surface vessel with a landing platform for UAVs consisting of a four-UPR parallel manipulator with three DoFs for wave synchronization. The estimation of the platform's DoFs was achieved using the well-established reciprocal screw theory. The mechanism can perform roll and pitch rotations as well as translations in the Z-axis. An inverse kinematics approach allowed a better understanding of how the variation of the parameters of the platform affects the mechanism properties. The workspace representation

was achieved with a numerical sweep that checks all the possible orientations for a given z of the upper platform. For $z = 0.5$ m, the platform pitch and roll combinations are limited to the area of a circle, given by Equation (28). The mechanism concept was further tested in a simulated scenario, resorting to ROS and Gazebo to emulate the physical model and environment. The inverse kinematics analysis and the use of a virtual chain were able to overcome the limitation of closed-loop chains in URDF files and achieve satisfying results in terms of the expected behaviour in these types of mechanisms. The control system applied in this work showed satisfying results for lower wave amplitudes (up to 0.4 m), with an η of 94.84%. This metric shows how well the top platform was able to sustain the horizontal position compared to the bottom one. However, for more aggressive sea states, the η starts dropping considerably, implying that a more robust control system is needed. Overall, the results achieved with this work show how wave synchronization in small surface vessels can be achieved with the methods demonstrated and the limitations imposed by the sea state.

Author Contributions: P.P., conceptualisation, validation, investigation, writing—original draft preparation; R.C., writing—review and editing, supervision; A.P., writing—review and editing, supervision, funding acquisition, project administration. All authors have read and agreed to the published version of the manuscript.

Funding: This work is funded by the European Commission under the European Union's Horizon 2020—The EU Framework Programme for Research and Innovation 2014–2020 under grant agreement No. 871571 (ATLANTIS).

Institutional Review Board Statement: Not applicable.

Informed Consent Statement: Not applicable.

Data Availability Statement: Not applicable.

Conflicts of Interest: The authors declare no conflict of interest.

Abbreviations

The following abbreviations are used in this manuscript:

UAV	Unmanned aerial vehicle
ASV	Autonomous surface vehicle
ROS	Robot operating system
R-joint	Revolute joint
U-joint	Universal joint
IMU	Inertial measurement unit
DoF	Degrees of freedom
URDF	Unified robot description format
PID	Proportional–integral–derivative

References

1. Lynch, K.M.; Park, F.C. *Modern Robotics: Mechanics, Planning, and Control*, 1st ed.; Cambridge University Press: Cambridge, MA, USA, 2017.
2. Ghobakhloo, A.; Eghtesad, M.; Azadi, M. Position control of a Stewart-Gough platform using inverse dynamics method with full dynamics. In Proceedings of the 9th IEEE International Workshop on Advanced Motion Control, Istanbul, Turkey, 27–29 March 2006; pp. 50–55.
3. Meng, X.; Gao, F.; Wu, S.; Ge, Q.J. Type synthesis of parallel robotic mechanisms: Framework and brief review. *Mech. Mach. Theory* **2014**, *78*, 177–186. [CrossRef]
4. Stewart, D. A platform with six degrees of freedom. *Proc. Inst. Mech. Eng.* **1965**, *180*, 371–386. [CrossRef]
5. Zhao, J.; Feng, Z.; Chu, F.; Ma, N. *Advanced Theory of Constraint and Motion Analysis for Robot Mechanisms*; Academic Press: Cambridge, MA, USA, 2013.
6. Merlet, J.P. *Parallel Robots*; Springer Science & Business Media: Berlin/Heidelberg, Germany, 2005; Volume 128.
7. Kong, X.; Gosselin, C. *Virtual-Chain Approach for the Type Synthesis of Parallel Mechanisms*; Springer: Berlin/Heidelberg, Germany, 2007.
8. Zhao, J.S.; Zhou, K.; Mao, D.Z.; Gao, Y.F.; Fang, Y. A new method to study the degree of freedom of spatial parallel mechanisms. *Int. J. Adv. Manuf. Technol.* **2004**, *23*, 288–294. [CrossRef]

9. Guan, L.W.; Wang, J.S.; Wang, L.P. Mobility analysis of the 3-UPU parallel mechanism based on screw theory. In Proceedings of the 2004 International Conference on Intelligent Mechatronics and Automation, Chengdu, China, 26–31 August 2004; pp. 309–314.
10. Wang, L.; Xu, H.; Guan, L. Mobility analysis of parallel mechanisms based on screw theory and mechanism topology. *Adv. Mech. Eng.* **2015**, *7*, 1687814015610467. [CrossRef]
11. Cai, J.; Deng, X.; Feng, J.; Xu, Y. Mobility analysis of generalized angulated scissor-like elements with the reciprocal screw theory. *Mech. Mach. Theory* **2014**, *82*, 256–265. [CrossRef]
12. Fang, H.; Fang, Y.; Zhang, K. Kinematics and workspace analysis of a novel 3-DOF parallel manipulator with virtual symmetric plane. *Proc. Inst. Mech. Eng. Part C J. Mech. Eng. Sci.* **2013**, *227*, 620–629. [CrossRef]
13. Zhang, H.; Fang, H.; Zhang, D.; Luo, X.; Zou, Q. Forward kinematics and workspace determination of a novel redundantly actuated parallel manipulator. *Int. J. Aerosp. Eng.* **2019**, *2019*, 4769174 . [CrossRef]
14. Pashkevich, A.; Chablat, D.; Wenger, P. Kinematics and workspace analysis of a three-axis parallel manipulator: The Orthoglide. *Robotica* **2006**, *24*, 39–49. [CrossRef]
15. Desai, R.; Muthuswamy, S. A forward, inverse kinematics and workspace analysis of 3RPS and 3RPS-R parallel manipulators. *Iran. J. Sci. Technol. Trans. Mech. Eng.* **2021**, *45*, 115–131. [CrossRef]
16. Laryushkin, P.; Antonov, A.; Fomin, A.; Essomba, T. Velocity and Singularity Analysis of a 5-DOF (3T2R) Parallel-Serial (Hybrid) Manipulator. *Machines* **2022**, *10*, 276. [CrossRef]
17. Du, X.; Wang, B.; Zheng, J. Geometric Error Analysis of a 2UPR-RPU Over-Constrained Parallel Manipulator. *Machines* **2022**, *10*, 990. [CrossRef]
18. Jones, T.; Dunlop, G. Analysis of rigid-body dynamics for closed-loop mechanisms—Its application to a novel satellite tracking device. *Proc. Inst. Mech. Eng. Part I J. Syst. Control. Eng.* **2003**, *217*, 285–298.
19. Wapler, M.; Urban, V.; Weisener, T.; Stallkamp, J.; Dürr, M.; Hiller, A. A Stewart platform for precision surgery. *Trans. Inst. Meas. Control* **2003**, *25*, 329–334. [CrossRef]
20. Ladenburg, J.; Hevia-Koch, P.; Petrović, S.; Knapp, L. The offshore-onshore conundrum: Preferences for wind energy considering spatial data in Denmark. *Renew. Sustain. Energy Rev.* **2020**, *121*, 109711. [CrossRef]
21. Campos, D.F.; Pereira, M.; Matos, A.; Pinto, A.M. DIIUS-Distributed Perception for Inspection of Aquatic Structures. In Proceedings of the OCEANS 2021: San Diego—Porto, San Diego, CA, USA, 20–23 September 2021; pp. 1–5.
22. Pinto, A.M.; Matos, A.C. MARESye: A hybrid imaging system for underwater robotic applications. *Inf. Fusion* **2020**, *55*, 16–29. [CrossRef]
23. Silva, R.; Matos, A.; Pinto, A.M. Multi-criteria metric to evaluate motion planners for underwater intervention. *Auton. Robots* **2022**, *46*, 971–983. [CrossRef]
24. Shafiee, M.; Zhou, Z.; Mei, L.; Dinmohammadi, F.; Karama, J.; Flynn, D. Unmanned aerial drones for inspection of offshore wind turbines: A mission-critical failure analysis. *Robotics* **2021**, *10*, 26. [CrossRef]
25. Pereira, P.N.D.A.A.D.S.; Campilho, R.D.S.G.; Pinto, A.M.G. Application of a Design for Excellence Methodology for a Wireless Charger Housing in Underwater Environments. *Machines* **2022**, *10*, 232. [CrossRef]
26. Aissi, M.; Moumen, Y.; Berrich, J.; Bouchentouf, T.; Bourhaleb, M.; Rahmoun, M. Autonomous solar USV with an automated launch and recovery system for UAV: State of the art and Design. In Proceedings of the 2020 IEEE 2nd International Conference on Electronics, Control, Optimization and Computer Science (ICECOCS), Kenitra, Morocco, 2–3 December 2020; pp. 1–6.
27. Li, W.; Ge, Y.; Guan, Z.; Ye, G. Synchronized Motion-Based UAV–USV Cooperative Autonomous Landing. *J. Mar. Sci. Eng.* **2022**, *10*, 1214. [CrossRef]
28. Liu, J.; Zhang, D.; Chen, Y.; Xia, Z.; Wu, C. Design of a class of generalized parallel mechanisms for adaptive landing and aerial manipulation. *Mech. Mach. Theory* **2022**, *170*, 104692. [CrossRef]
29. Guo, J.; Li, G.; Li, B.; Wang, S. A ship active vibration isolation system based on a novel 5-DOF parallel mechanism. In Proceedings of the 2014 IEEE International Conference on Information and Automation (ICIA), Hailar, China, 28–30 July 2014; pp. 800–805. [CrossRef]
30. Chen, B.Y.; Chiang, M.H. Simulation and experiment of a turbine access system with three-axial active motion compensation. *Ocean Eng.* **2019**, *176*, 8–19. [CrossRef]
31. Cai, Y.; Zheng, S.; Liu, W.; Qu, Z.; Zhu, J.; Han, J. Sliding-mode control of ship-mounted Stewart platforms for wave compensation using velocity feedforward. *Ocean Eng.* **2021**, *236*, 109477. [CrossRef]
32. Pinto, A.M.; Marques, J.V.A.; Campos, D.F.; Abreu, N.; Matos, A.; Jussi, M.; Berglund, R.; Halme, J.; Tikka, P.; Formiga, J.; et al. ATLANTIS—The Atlantic Testing Platform for Maritime Robotics. In Proceedings of the OCEANS 2021, San Diego—Porto, San Diego, CA, USA, 20–23 September 2021; pp. 1–5. [CrossRef]
33. Zhao, T.S.; Li, Y.W.; Chen, J.; Wang, J.C. A Novel Four-DOF Parallel Manipulator Mechanism and Its Kinematics. In Proceedings of the 2006 IEEE Conference on Robotics, Automation and Mechatronics, Bangkok, Thailand, 7–9 June 2006; pp. 1–5. [CrossRef]
34. Neves, F.S.; Claro, R.M.; Pinto, A.M. End-to-End Detection of a Landing Platform for Offshore UAVs Based on a Multimodal Early Fusion Approach. *Sensors* **2023**, *23*, 2434. [CrossRef]
35. Bingham, B.; Agüero, C.; McCarrin, M.; Klamo, J.; Malia, J.; Allen, K.; Lum, T.; Rawson, M.; Waqar, R. Toward maritime robotic simulation in gazebo. In Proceedings of the OCEANS 2019, Seattle, WA, 27–31 October USA, 2019; pp. 1–10.

36. Thon, S.; Dischler, J.M.; Ghazanfarpour, D. Ocean waves synthesis using a spectrum-based turbulence function. In Proceedings of the Computer Graphics International 2000, Geneva, Switzerland, 19–24 June 2000; pp. 65–72.
37. Halvorsen, H.S.; Øveraas, H.; Landstad, O.; Smines, V.; Fossen, T.I.; Johansen, T.A. Wave motion compensation in dynamic positioning of small autonomous vessels. *J. Mar. Sci. Technol.* **2021**, *26*, 693–712. [CrossRef]